Continental Shelf Research 30 (2010) 1149–1165

Contents lists available at ScienceDirect

Continental Shelf Research

journal homepage: www.elsevier.com/locate/csr

Temporal observations of rip current circulation on a macro-tidal beach

Martin Austin [a,*], Tim Scott [a], Jeff Brown [b], Jenna Brown [c], Jamie MacMahan [c], Gerd Masselink [a], Paul Russell [a]

[a] School of Marine Science and Engineering, University of Plymouth, Drake Circus, Plymouth PL4 8AA, UK
[b] Center for Applied Coastal Research, University of Delaware, Newark, DE, USA
[c] Oceanography Department, Naval Postgraduate School, Monterey, CA, USA

ARTICLE INFO

Article history:
Received 2 December 2009
Received in revised form
26 February 2010
Accepted 10 March 2010
Available online 18 March 2010

Keywords:
Rip current
Macro-tidal
Surf zone
Intermediate beach
Drifters
Cell circulation

ABSTRACT

A field experiment was conducted on a high energy macro-tidal beach (Perranporth, UK) to examine rip current dynamics over a low-tide transverse bar/rip system in response to changing tide and wave conditions. Hydrodynamic data were collected using an array of in situ acoustic doppler current meters and pressure transducers, as well as 12 GPS-tracked Lagrangian surf zone drifters. Inter-tidal and sub-tidal morphology were measured through RTK-GPS and echo-sounder surveys. Data were collected for eight consecutive days (15 tides) over a spring-neap tidal cycle with tidal ranges of 4–6.5 m and offshore significant wave heights of 1–2 m and peak periods of 5–12 s.

The hypothesis that rip current dynamics in a macro-tidal setting are controlled by the combination of variations in wave dissipation and morphological flow constriction, modulated by changes in tidal elevation was tested. During the measurement period, rip circulation was characterised by a large rotational surf zone eddy O(200 m) extending offshore from the inner-surf zone to the seaward face of the inter-tidal transverse bar. During high- and mid-tide, water depth over the bars was too deep to allow wave breaking, and a strong longshore current dominated the surf zone. As the water depth decreased towards low-tide, wave breaking was concentrated over the bar crests initiating the rotational rip current eddy. Peak rip flow speeds of 1.3 m s^{-1} were recorded around low-tide when the joint effects of dissipation and morphological constriction were maximised. At low tide, dissipation over the bar crests was reduced by partial bar-emergence and observations suggested that rip flows were maintained by morphological constriction and the side-drainage of water from the transverse bars.

1. Introduction

Previous investigations into beach hazards in the UK, Australia and the USA have indicated that rip currents present the single most significant cause of rescues and fatalities for recreational beach users (e.g. Short and Brander, 1999; Scott et al., 2007, 2008). Scott et al. (2008) identified that 68% of all incidents recorded by the Royal National Lifeboat Institution (RNLI) on UK beaches were due to rip currents. Furthermore, over 90% of recorded UK rip incidents were shown to occur on beaches with identifiable rip channel morphologies (i.e. low tide bar/rip and low tide terrace + bar/rip). During periods of high rip current activity, environmental controls present an 'optimum' combination of beach morphological state (bar/rip morphology) and prevailing hydrodynamic conditions (waves and tides) (Scott et al., 2009). Combined with the tide-induced temporal variation of the beach hazard signature, these optimum conditions are observed to be a key factor in driving periods of high beach risk during busy summer months, which have been shown to be associated with coast-wide mass rescue events.

Rip currents are a well studied phenomenon in micro- and meso-tidal environments (e.g. Shepard et al., 1941; McKenzie, 1958; Bowman et al., 1988; Huntley et al., 1988; Brander, 1999; Brander and Short, 2001; MacMahan et al., 2005, 2006) and have been shown to form an integral component of nearshore cell-circulation, returning water seawards from within the surf zone, largely as a confined energetic jet. Increasing interest and technological capability within the past decade have led to a greater number of quantitative studies of rip current dynamics; however, macro-tidal environments have been largely ignored with the recent exception of Bruneau et al. (2009) who investigated rip currents at a site spanning the meso–macro-tidal transition.

The presence of rip currents is most commonly associated with intermediate-type beach morphology (Wright and Short, 1984) and in macro-tidal environments the effect of the tide is significant in shaping this morphology (Masselink and Short, 1993). Specifically, macro-tidal beaches frequently display a propensity to form rhythmic bar and trough systems during periods of smaller waves in the region seaward of mean low water neaps (MLWN) where

* Corresponding author. Tel.: +44 1752584716.
E-mail address: martin.austin@plymouth.ac.uk (M. Austin).

0278-4343/$ - see front matter
doi:10.1016/j.csr.2010.03.005

there is sufficient tidal stationarity within a high-energy environment to allow bar/trough systems to develop. The semi-rhythmic form of the inter-tidal bars results in a morphology characterised by shallow shore-connected shoals incised by deeper rip channels. This leads to considerable longshore non-uniformity, variations in wave breaking and in turn cross- and longshore gradients in the radiation stress and the mean water surface driving water from the bars towards the channels (Bowen, 1969). The degree of morphological development thus becomes a key factor in determining the flow kinematics of a macro-tidal rip system and hence rips are frequently modulated at a seasonal scale (e.g. Brander, 1999).

Rip currents are known to be modulated by tide-induced changes in water depth with decreases in tidal stage increasing rip current flows to a relative maximum (e.g. Aagaard et al., 1997; Brander, 1999; Brander and Short, 2000, 2001; MacMahan et al., 2005, 2006; Bruneau et al., 2009). This modulation has been linked to temporal changes in the expression of the morphology causing: (1) spatial and temporal variation in the pattern of wave dissipation; and (2) morphological flow constriction.

Sonu (1972), Haller et al. (2002) and MacMahan et al. (2006) state that wave breaking over nearshore bars is essential for the formation of rip circulation and that the intensity of breaking corresponds with a proportionally stronger circulation. Considering the case of low tide bar/trough morphology, at high- and mid-tide the amount of wave dissipation over the bars will be small and hence the alongshore set-up gradient is small. Conversely, at low tide, increased dissipation over the bar crests forces a large alongshore set-up gradient, water flows alongshore landwards of the bar crests, converging in the incised channels before flowing seawards—the rip current is now active. At some critical level of water depth over the bar, the set-up gradient and hence rip current flow will be maximised.

Brander (1999) presents a conceptual model whereby the morphodynamic behaviour of rip currents is placed within the context of the Wright and Short (1984) beach state model with down-state transitions linked to strengthening rip flows. The onset of transverse bar/rip morphology (TBR) sees the infilling of the longshore feeder channels, amplifying the morphological expression of the rip channel and thus maximising the rip speed. Short (1985) hypothesizes that flow velocity is stable whilst constrained within the channel, but that once the banks are overtopped with increasing water depth the flow dramatically reduces. Moreover, Brander and Short (2001) suggest that topographic confinement enhances rip flow at lower tidal stages with the observation that narrow rip channels with pronounced banks were more sensitive to tidally induced water depth changes.

Spatial and temporal variations in the distribution of wave dissipation and morphological flow constriction both have the potential to modulate rip current flow in a macro-tidal environment. The purpose of this paper is to describe and quantify the dynamic behaviour of a macro-tidal rip current system to test whether one process is dominant, or alternatively whether both processes are collectively responsible for the observed rip modulation. We use both Lagrangian and Eulerian field data collected from a high-energy macro-tidal beach during a period of large spring tides and moderate waves to provide detailed measurements from within a rip current as well as the synoptic overview of the entire system at a time when the rip hazard signature was at its seasonal maximum.

2. Methodology

2.1. Study site

An 8-day field experiment was conducted at Perranporth beach, Cornwall, UK over a spring-to-neap tidal cycle between 01 and 08 August 2008 (Fig. 1). Perranporth is a macro-tidal beach with semi-diurnal tidal regime and a mean spring range of 6.3 m. It falls at the transition between the low tide bar/rip and dissipative beach states and exhibits pronounced low tide bar/rip morphology which varies on a seasonal timescale. The intertidal beach is relatively flat ($\tan\beta = 0.015$–0.025) and the beach is composed of medium quartz sand ($D_{50} = 0.28-0.34$ mm). The beach faces west-northwest and is predominantly exposed to Atlantic swell, but also receives locally generated wind waves; it has an annual average significant wave height and peak period of $H_s = 1.6$ m and $T_p = 10.5$ s, respectively.

2.2. Field methods and instrumentation

The intertidal beach elevation was surveyed at low tide from the cliff foot to ~ 0.2 m water depth using a real time kinematic GPS (RTK-GPS) mounted on an all-terrain vehicle (ATV) at the start and end of the experiment. Additional lower-intertidal surveys were performed during tides 3, 7, 9 and 13. A bathymetric survey was conducted during high tide 13–14 using RTK-GPS and an echo-sounder mounted on an RNLI inshore rescue boat to a depth of 16 m and overlapping with the intertidal survey. Data were Loess-interpolated onto a regular grid and transformed into a local coordinate system [X,Y], where X is directed cross-shore and increases to seaward and Y is alongshore increasing to the south (Fig. 2). An Argus video system was also located at Perranporth. Time-averaged images were recorded every 30-min and merged and rectified onto the same local coordinate system as the bathymetric measurements.

An array of in situ sensors were deployed around the mean low water spring (MLWS) tidal level to monitor the rip current flows (Fig. 2). Flow velocity and water depth within the rip channel and adjacent incised shore-parallel low-tide bar/feeder region were measured with Nortek Vector 3D-ADV's equipped with an external pressure transducer (PT). The head of the ADV's and co-located sensors were mounted 0.2 m above the bed. The instruments were mounted onto free-standing frames and were deployed between tides 3 and 9. The frames were removed after tide 9 since the waning tidal range would have prevented recovery until the following month. An RBR-instruments TWR2050 self-recording tide-wave recorder (TWR) located on the crest of the intertidal bar recorded water depth for 2048-sample bursts every 10 min. Tidal elevation data were also predicted through harmonic analysis of previous data from the field site. All instruments sampled at 4 Hz. In addition, a directional wave rider (DWR) buoy located ~ 1.2 km offshore in 13 m water depth provided offshore wave measurements throughout the field experiment.

The surf zone circulation associated with rip current flows was measured using Lagrangian drifters. Rip drifter floats were constructed following a design similar to Schmit et al. (2003) and their position was monitored at 0.5 Hz using GPS loggers that were post-processed from a survey-grade static base station following MacMahan et al. (2009). These provided estimates of rip current flows with an accuracy for position and speed of < 0.4 m and < 0.01 m s^{-1}, respectively. MacMahan et al. (2009) also compared drifter and dye releases indicating that drifter observations are valid Lagrangian observations as well as comparing well with in situ observations. The positional data were quality controlled to remove erroneous points (greater than three velocity standard deviations from the mean) and gaps in the time series were linearly interpolated when > 10 s and spline interpolated when < 10 s, consistent with drifter observations by Spydell et al. (2007). Drifters were released into the surf zone in clusters of 4 and allowed to circulate with the currents until they

Fig. 1. Location map of Perranporth indicating the experimental region (circled) and DWR buoy.

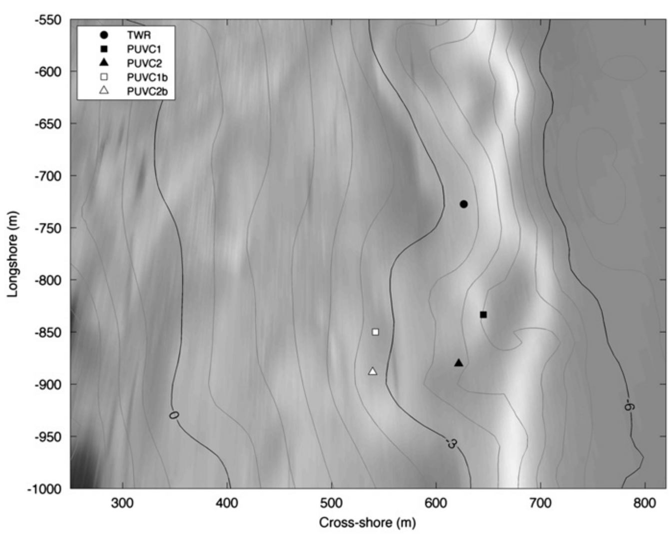

Fig. 2. Bathymetry and instrument rig locations. Contours plot the combined inter- and sub-tidal bathymetry measured during LT 13 relative to Ordnance Datum Newlyn (mODN) at 0.5 m intervals. Black contours indicate MSL and MLWS. The figure background is the low tide Argus video intensity image indicating the regions of wave dissipation (white) and hence bar configuration in the surf zone.

either grounded at the shoreline or escaped from pre-defined longshore and offshore boundaries.

3. Data processing

3.1. Hydrodynamic data

The continuous data collected by the in situ hydrodynamic instruments (time series of water depth h, cross- and longshore flow velocity u and v) were calibrated, de-spiked and organised into coincident 8.5-min bursts (2048-samples) every 10-min. The time series of u was used to calculate the root mean square orbital velocity U_m ($=\sqrt{8}\sigma_u$, where σ_u is the standard deviation of the cross-shore velocity record) and the mean flow velocity $\langle u \rangle$ (where brackets represent time-averaging); similar longshore parameters were calculated for v. Using the hydrodynamic indicators calculated above, the Froude number F_r was defined as a non-dimensional measure of rip speed (Haller et al., 2002)

$$F_r = \frac{U_r}{\sqrt{gh}}, \tag{1}$$

where U_r is the mean return speed ($=\sqrt{\langle u \rangle^2 + \langle v \rangle^2}$), g is the gravitational acceleration and h the local water depth over the bar crest, in line with previous field and laboratory experiments. Parameters were removed from the analysis when individual sensors became emerged.

The relative wave height H_s/h provides a useful measure of wave breaking within the nearshore zone (Ruessink et al., 1998) and has been used in previous rip studies as a proxy for wave dissipation. H_s/h can be computed using the offshore wave height at the DWR, $H_{s,DWR}/h_{bar}$ (e.g. MacMahan et al., 2005, 2006) or in a local form using the water depth measured on the crest of the intertidal bar $H_{s,bar}/h_{bar}$; however, both of these approaches can be problematic in a macro-tidal environment if the crest of the inter-tidal bar emerges at low water. In this situation, $H_{s,DWR}/h_{bar} \to \infty$ as un-attenuated offshore waves 'propagate' into near-zero water depth on the bar. For the local case, $H_{s,bar}/h_{bar} \to 0$ as the water depth goes to zero at the shoreline but, across the isolated swash zone that develops on the bar crest, also tends to ∞ as large broken wave bores intermittently propagate across the dry crest. In an attempt to avoid these problems when quantifying the large spatial and temporal variations in rip flow recorded by the Lagrangian drifters an alternative parameterisation, the wave roller dissipation, was estimated from the remote video observations.

3.2. Wave roller dissipation

Estimates of the wave roller dissipation were obtained from the plan view Argus timex images of wave breaking intensity combined with the inshore water depth and wave height. The quantification procedure largely follows the method of Aarninkhof et al. (2005) and van Dongeren et al. (2008) and assumes that video intensity is a proxy for roller dissipation.

Firstly, the background intensity level is removed from the merged plan view dissipation map (timex image) I_v, since the offshore areas (where no breaking occurs) should map to no wave dissipation (zero video intensity). This is achieved by determining the mean image intensity for each horizontal image line along the seaward boundary (non-breaking) of the domain in the region $x=750-800$ m and subtracting this value from each image line across the entire domain; negative intensities are set to zero.

Secondly, the corrected image intensities are scaled such that they provide a quantitatively correct measure of roller dissipation. Accordingly, I_v is normalised so that the total normalised intensity in the domain equals unity and then scaled with the incoming wave energy flux along the seaward boundary of the domain, thereby providing a video-derived measure of roller dissipation D_0

$$D_0(x,y) = \left(\frac{I_v(x,y)}{\int_x \int_y I_v \, dx \, dy} \right) \int_y E C_g \cos\theta \, dy, \tag{2}$$

where E is the wave energy at the DWR according to $E = 1/8 \rho g H_{rms}^2$, C_g is the wave group velocity and θ is the angle of wave incidence with respect to the shoreline. H_{rms} and θ were obtained from the DWR.

An example low tide roller energy dissipation map is shown in Fig. 3. Strong roller dissipation is evident across the low tide transverse bar system and across the offshore limit of the rip head regions; further landwards, roller dissipation is also present along the edges of the shore-connected shoal and into the swash zone. Within the rip channels the degree of roller dissipation is very low, indicative of limited wave breaking.

Since longshore gradients in nearshore momentum fluxes are important in driving rip currents and in order to provide a temporal measure of the energy dissipation in the nearshore, the alongshore gradient in roller dissipation dD_0/dy between the bar crest and rip channel was computed as

$$dD_0/dy = \frac{D_{0,bar} - D_{0,rip}}{dy}, \tag{3}$$

where $D_{0,bar}$ and $D_{0,rip}$ are the 30-min average dissipation over the bar crest and rip channel, respectively, and dy is the longshore separation between the bar and rip ($dy = 122$ m). The roller dissipation gradient was computed for every available Argus image during the field experiment (every 30-min during daylight hours).

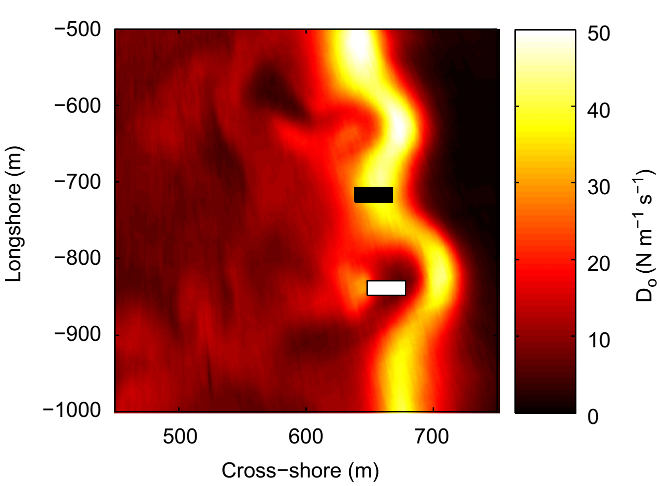

Fig. 3. Merged plan view roller dissipation map over the rip current system derived from video observation during 04 August. The black and white patches indicate the dissipation averaging regions over the bar crest and rip channel, respectively.

4. Results

The analysis of six coast-wide mass rescues of beach users from rip currents in the southwest UK during 2007 identified that the small long-period swell waves, large tidal ranges and well developed low tide bar/trough morphology that are prevalent during the peak mid-summer holiday season were key environmental factors in these rescues (Scott et al., 2009). Therefore in order to better understand the driving mechanisms of macro-tidal rip current systems representing the highest hazard signature to beach users, it was critical to perform the experiment under the above conditions. To maximise the probability of collecting observations under these conditions, the beach morphology was monitored for a three month period prior to the experiment. Held during July–August 2008, the experiment coincided with large spring tides and summer swell conditions, with an extensive low tide transverse bar/rip system.

4.1. Tide and wave climate

During the field experiment, morphological and hydrodynamic data were collected during 15 tidal cycles (LT 1–15) centred over the peak spring tide period with tidal ranges in excess of 6 m (Fig. 4). The predicted tides closely match those recorded by the TWR in both phase and amplitude. H_s and T_p were 1–2 m and 5–12 s, respectively, and were similar at both the bar crest and DWR locations, which is indicative of swell conditions. During tide 14–15, T_p reduced sharply as strong NW winds caused local wave generation. The average peak wave direction recorded by the DWR is -19° (left of shore normal), except for during periods of local wave generation when it is $\approx 0^\circ$. Although the swell waves approach slightly oblique to the shoreline, refraction due to the local bathymetry between the DWR and the shoreline create near-normal incidence and results in weak or non-existent net longshore currents. Table 1 summarises the conditions throughout the experiment and highlights the waning tidal range from the spring tide peak during LT 3.

The time series of the video-derived wave roller energy dissipation D_0 over the bar crest and rip channel regions is shown in Fig. 5. As expected, the wave energy flux P follows a very similar trend to H_s, being generally greater during the second half of the experiment, but due to the daylight constraints of the Argus system, the roller dissipation is only available for alternate tides. D_0 varies between 0 and 70 N m^{-1} s^{-1} but it is observed to peak around low water at both bar and rip locations as wave breaking occurs across the low-tide beachface. $D_{0,bar}$ and $D_{0,rip}$ follow similar trends and although $D_{0,bar}$ is generally greater than $D_{0,rip}$ at low water (particularly during LT 7), there are periods when roller dissipation is equal across the bar and rip channel (i.e. LT 13). Two additional side-lobe peaks are obvious either side of low water and these are probably due to the low angle of the sun around sunrise and sunset. Unfortunately, due to the orientation of the two cameras, the horizon is not visible in both image frames so the image intensities cannot be sufficiently balanced prior to producing the merged plan view. During the periods of drifter deployment, the longshore gradient in roller dissipation dD_0/dy is $O(0.01–0.1)$ and generally directed towards the rip indicating as expected that there is stronger dissipation over the bar. However, during LT 3 and LT 13, dD_0/dy is negative, suggesting that there is greater roller dissipation in the rip channel than over the bar

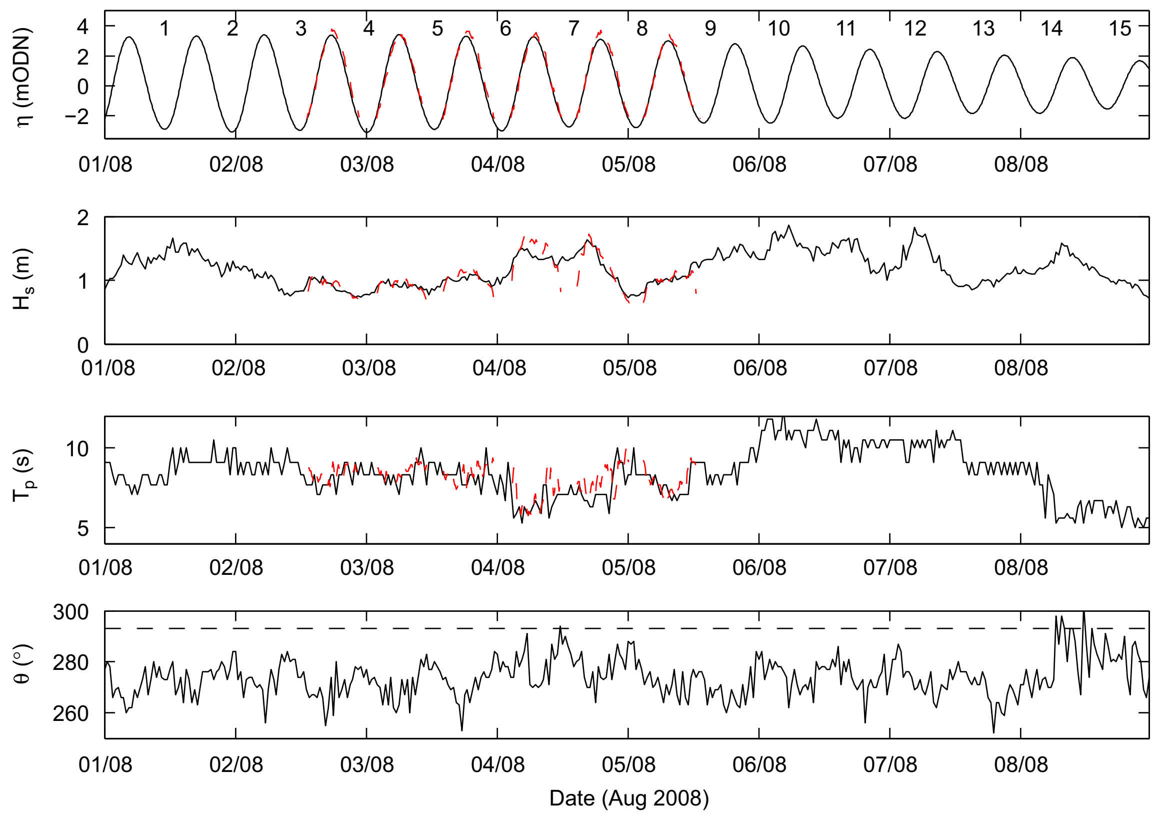

Fig. 4. Offshore and nearshore wave conditions during the field experiment. (From top) Tidal level obtained from TWR (dash) and predictive model (solid); significant wave height H_s; peak wave period T_p; and peak wave direction θ. Dashed and solid lines indicate data measured by inshore TWR offshore DWR, respectively. The dashed horizontal line in the lower plot indicates shoreline orientation.

Table 1
Summary of hydrodynamic conditions experienced during the drifter deployments.

LT number	H_s (m)	T_p (s)	θ (°)	η (m)
3	0.83	8.3	274	6.35
5	0.84	9.1	280	6.20
7	1.31	7.1	286	5.97
9	1.32	9.1	272	5.47
13	0.85	9.1	271	4.12

Shoreline orientation is 293°, so θ−293° provides wave direction relative to shore normal (negative is left of shore normal).

crest. The additional side-lobe peaks from above are also clearly present in dD_0/dy.

$H_{s,DWR}/h_{bar}$ has been used previously as a proxy for wave dissipation within the surf zone with which to quantify rip circulation (e.g. MacMahan et al., 2005, 2006). D_0 provides an alternative and quantitatively correct measure of the actual roller dissipation and should provide a similar temporally varying signal provided that $H_{s,DWR}/h_{bar}$ fully incorporates the wave energy dissipation due to wave breaking. To compare $H_{s,DWR}/h_{bar}$ and D_0 a continuous time series of h is required from the bar crest, but since this was not available due to the bar drying at low tide, the missing data were replaced by interpolating the local predicted tidal elevation after this was corrected for a small phase offset by cross-correlating it with the measured elevation. Comparing the two parameters, it is clear that while both parameters generally follow the same trend, $H_{s,DWR}/h_{bar}$ does not significantly differentiate between LT 5 and 7 or LT 9 and 11, whereas D_0 is appreciably different for those tides; this is possibly a reflection of the variations in wave period not encapsulated within $H_{s,DWR}/h_{bar}$.

4.2. Beachface morphology

The beachface morphology was characterised by an extensive transverse bar system with incised rip channels located just below the MLWS elevation (Fig. 2). The incised channels were quasi-periodic with a spacing $O(250\,\text{m})$. The crest of the transverse bar was located at $[X,Y]=[630,-725\,\text{m}]$ with a prominent rip channel running diagonally from the end of the bar $[X,Y]=[680,-900\,\text{m}]$ seawards towards $[X,Y]=[600,-775\,\text{m}]$. The neighbouring transverse bar formed a prominent shoal at $Y=-950\,\text{m}$. The low tide Argus intensity image clearly identifies the extent of the surf zone and indicates that waves are breaking on the seaward slope of the transverse bars and across the seaward limit of the incised rip channels.

To clearly identify the regions of positive and negative relief within the rip system, the underlying beach slope was removed by subtracting a linear trend surface from the intertidal bathymetric survey to leave the residual morphology (Fig. 6a). The crest of the intertidal bar is clearly identified at $[X,Y]=[620,-725\,\text{m}]$, and the shore-connected shoal at $[X,Y]=[720,-860\,\text{m}]$ appears to constrain the rip circulation in the longshore. This shoal also appears to merge with the offshore sub-tidal bar. Significantly, there is a relatively deep incised channel between these two regions of positive relief, which constitutes the rip neck area, and no evidence of a rip-head bar. Since the bar/trough morphology is located on the intertidal beachface, changing tidal elevation alters the effective morphologic area of these bars and modulates their effect on the rip circulation.

To quantify this temporal signal, the morphological cross-sectional area of the rip channel A_m was computed (Fig. 6b). This was defined across a longshore transect, at the cross-shore location of the TWR, between the points of maximum residual

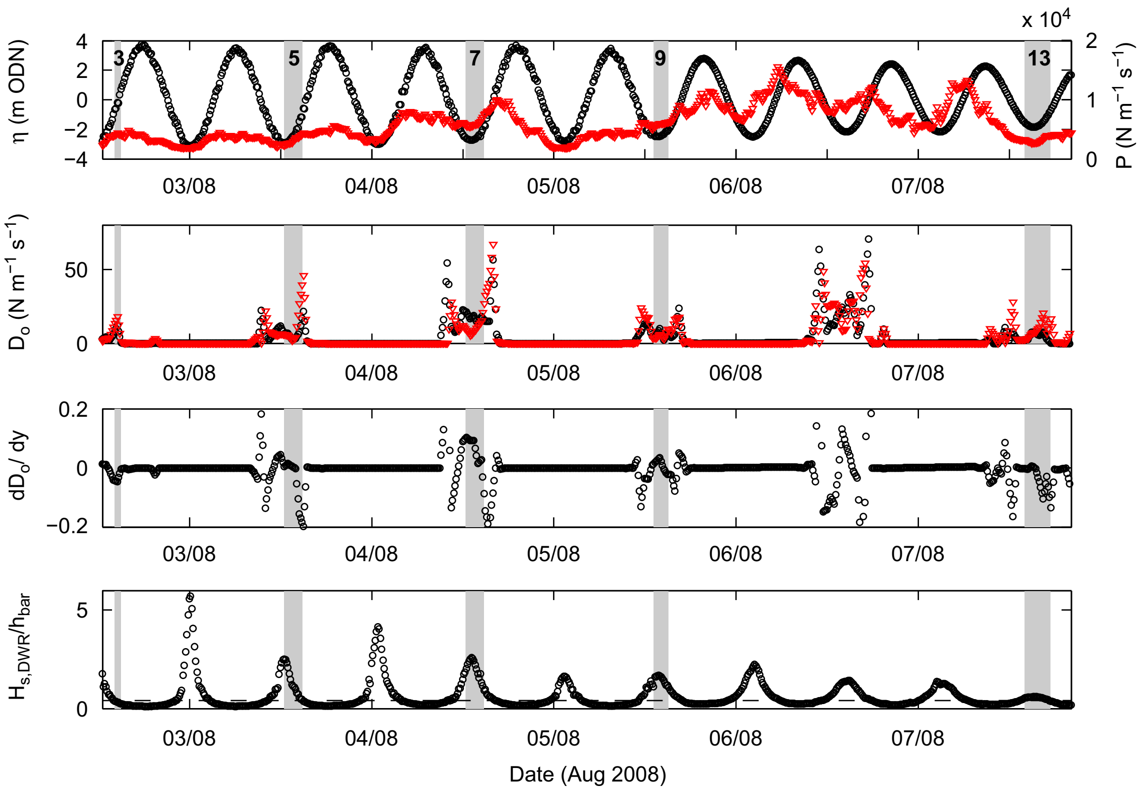

Fig. 5. Time series of wave energy roller dissipation. (From top) Tidal elevation η (circle), and wave energy flux P at cross-shore position $X=800$ m (triangle); wave energy roller dissipation over the bar (circle) and rip channel (triangle); longshore roller dissipation gradient and (bottom) H_s/h computed with H_s measured at the DWR. Shaded regions indicate drifter deployments.

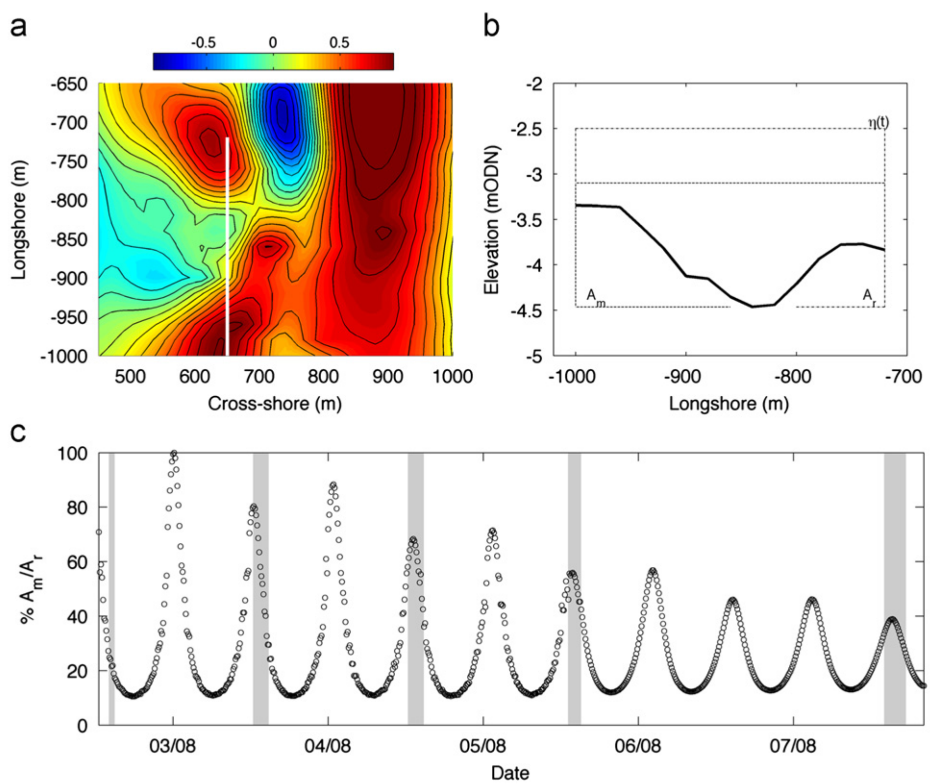

Fig. 6. Morphological characteristics of the rip channel. (a) Residual morphology highlighting areas of positive (red) and negative (blue) relief and indicating the cross-section through the rip channel (white line). (b) Example cross-section through the rip channel indicating the derivation of the area available for rip flow A_r and the morphological area of the channel A_m. (c) Temporal variation in the percentage of A_m/A_r. Shaded regions indicate the periods of rip drifter deployment. (For interpretation of the references to colour in this figure legend, the reader is referred to the web version of this article.)

morphological relief of the intertidal bar and shore-connected shoal (cf. Brander, 1999), with the vertical limit defined as the minimum tidal elevation recorded during the experiment $\eta_m(=-3.1\ \mathrm{mODN})$

$$A_m = \int_{y=1}^{y=n} (z+\eta_m)\,dy. \tag{4}$$

The total area available for rip current flow A_r was also defined, where $\eta(t)$ is the measured tidal elevation

$$A_r(t) = \int_{y=1}^{y=n} (z+\eta(t))\,dy. \tag{5}$$

The percentage of A_m to A_r provides a quantitative measure of the morphological constriction placed on the rip circulation by the channel morphology (Fig. 6c).

4.3. Eulerian rip current flows

The in situ instruments were deployed below the MLWS elevation and the water depth over each tide typically varied between 0.5 and 7 m (Fig. 7). The significant wave height was $O(1\ \mathrm{m})$, but increased to 1.5–2 m during LT 7–8. The wave height was modulated by the variation in water depth and this was most apparent over the bar rather than the deeper rip/feeder regions. The relative wave height H_s/h provides an indication of wave breaking and suggests that during low tide wave breaking occurs at all instrument stations ($H_s/h>0.6$); however, the lowest proportion of breaking occurs in the rip channel. This is particularly evident during LT 3–5, when there is significant wave breaking across the bar crest and feeder regions, but minimal breaking across the rip channel. Note that H_s/h over the bar crest is discontinuous around low tide as the bar crest emerges.

The flow velocity data display significant tidal modulation of the currents with maximum flows recorded around low water at both the feeder and rip locations (Fig. 8). Cross-shore orbital velocities were 0.5–1.5 $\mathrm{m\,s^{-1}}$, while the mean cross-shore currents $\langle u \rangle$ were generally offshore and reach $-0.5\ \mathrm{m\,s^{-1}}$. Mean longshore currents $\langle v \rangle$ were recorded up to 0.5 $\mathrm{m\,s^{-1}}$ to both the north and south. Due to the circulation present around the bar/rip, flow was not always directed in either a cross- or longshore direction so the mean return speed U_r was computed and indicates that maximum U_r coincides with low tide.

The mean current velocities display a clear dependence on the local water depth (tidal elevation) (Fig. 9). Mean cross-shore currents become increasingly offshore-directed once the water depth falls below ~ 3 m, and while the longshore currents are observed to flow in both directions, they are of a similar magnitude to the cross-shore flows. There appears to be little differentiation between the magnitude of the mean currents during the flood and ebb tide periods.

Due to varying conditions on each day of the experiment, rip current speeds display some dependence on wave energy. Therefore using the dimensionless rip current velocity parameterised as the Froude number (Eq. (1)), rip speed scales well with the relative wave height, displaying a strong linear relationship with r values of 0.77 and 0.86 for feeder and rip locations, respectively. Note that D_0 could not be used here since it was only sampled at 30-min intervals so the relative wave height at the bar crest was used ($H_{s,bar}/h_{bar}$), rather than the offshore wave height alternative as used by MacMahan et al. (2005).

An alternative scaling relationship was proposed by Brander and Short (2001). To account for changing wave energy levels between tides, U_r is normalised by the wave steepness H_s/T_p and to account for varying tidal elevations, h was normalised by the high tide water depth h_{ht}. Fig. 10 shows that U_r is strongly modulated by the water depth indicating that rip speed increases with decreasing water depth, particularly after mid-tide (h/h_{ht}). An exponential fit, as suggested by Brander and Short (2001) models the data reasonably well, however, it underestimates the flow speeds at high water and overestimates the mid-tide speeds.

4.4. Lagrangian drifter observations

4.4.1. Mean circulation

Lagrangian observations obtained using GPS drifters during LT 3, 5, 7, 9 and 13 quantify the rip circulation pattern and speed over a large spatial area of the system compared to the in situ Eulerian measurements. The nearshore was split into 10 m × 10 m bins and the drifter observations during each deployment were averaged within each bin. A drifter was considered as an independent observation when within a particular bin. If a drifter re-entered the same bin it was considered a new independent observation if $t>l_g/U$ had elapsed, where t is time, l_g is the bin length (10 m) and U is the mean speed for all drifter observations within that bin (MacMahan et al., 2010a). Bins containing greater than 5 independent observations were considered statistically significant following Spydell et al. (2007).

It is clear that a large rotational rip circulation system was present within the surf zone during periods of the field experiment with cross- and longshore length scales $O(200\ \mathrm{m})$ (Fig. 11). The rip circulation was anti-clockwise and flowed offshore through the surf zone under an angle of $\sim 45^{\circ}$ until reaching the seaward breaker line. The flow then turned longshore for ~ 75 m before returning landwards over the shallow intertidal bar at $[X,Y]=[650,-750\ \mathrm{m}]$. Additionally, there are several points during the circulation where drifters would sometimes exit the surf zone to seawards, be incorporated into adjacent circulation cells or meander into very shallow water to landwards.

The rotational eddy was present with varying degrees of persistence and speed for all tides except LT 13. The most highly developed circulation cells were present during LT 5 and LT 7; conversely, LT 9 and LT 13 are dominated by alongshore currents with very limited rotational circulation. The significant mean flow speeds recorded by the drifters from within the circulation system are $0.01-1.27\ \mathrm{m\,s^{-1}}$, with maximum speeds coincident with the strongest circulation during LT 5 and LT 7. Modal drifter speeds during the deployment ranged from 0.3 to 0.5 $\mathrm{m\,s^{-1}}$ and were comparable with the Eulerian speeds ($0.35-0.4\ \mathrm{m\,s^{-1}}$); however, due to the large spatial area covered by the drifters the standard deviation of rip speeds ($\sigma_L=0.19$) is greater than for the in situ measurements ($\sigma_E=0.07$). It seems clear that when the rip current is active, the flow is circulatory in nature; conversely, when the longshore motion is dominant there is little or no offshore-directed flow through the rip channel.

4.4.2. Kinematic circulation control

To investigate the nature of the rip current circulation under a range of tide conditions all drifter observations were combined and classified according to the local water depth on the bar crest h_{bar} measured at the time of drifter release (Fig. 12). The two previously identified modes of rip circulation appear to be differentiated by variations in h. For shallow water depths ($h<$ 1.8 m) strong rotational circulation is present, while for $h>1.8$ m the alongshore current dominates and there is little offshore flow through the rip channel. The alongshore directed flows from the bar crest to the landward end of the rip channel are consistently the strongest, reaching $0.7-1\ \mathrm{m\,s^{-1}}$. It is also noted that the drifter circulation pattern is shifted slightly landwards as water depths increase, reflecting the shoreline migration.

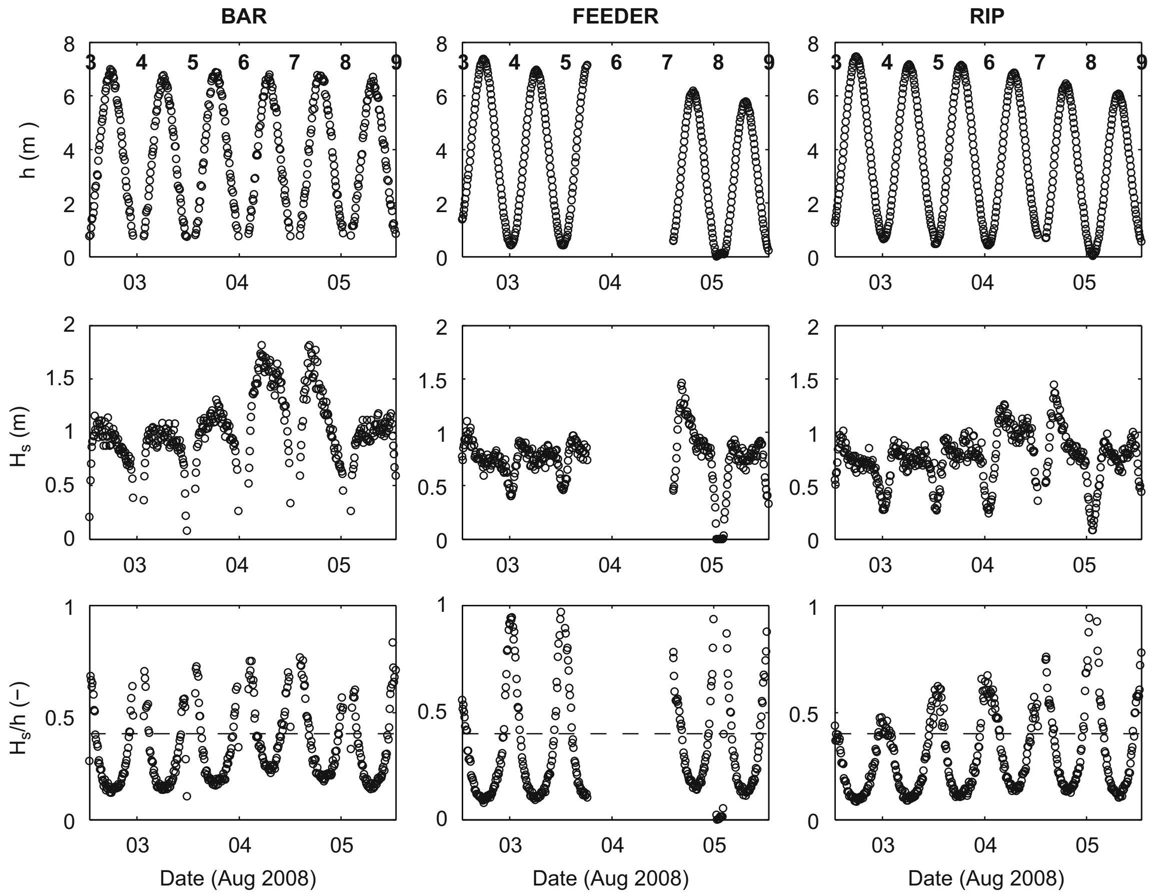

Fig. 7. Summary of the pressure statistics measured by the in situ instruments at 10-min intervals. (From top) Water depth h; significant wave height H_s; and local relative wave height H_s/h. The dashed line in the lower panels indicates the onset of wave breaking at $H_s/h > 0.4$.

4.4.3. Dynamic circulation control

While it is obvious that the synoptic pattern of rip circulation is modified by tide-induced changes in water depth, it remains unclear whether the physical process forcing the rip circulation is wave energy dissipation or morphological flow constriction. To assess the relative importance of these two processes the drifter data are combined and class-averaged according to the longshore gradient in wave roller energy dissipation dD_0/dy and the relative morphological cross-section of the rip channel A_m/A_r.

Fig. 13 plots the synoptic drifter circulation pattern averaged over dD_0/dy classes for both the statistically significant data and, with the requirement for >5 independent observations relaxed, all the data. There appears to be a tendency for the strongest rip flow speeds to occur when dD_0/dy is directed towards the rip channel, consistent with a set-up gradient acting towards the rip channel. Also, for the significant drifter data dD_0/dy seem to have some skill in discriminating between rotational and longshore circulation, with significant rotation only occurring for $dD_0/dy \geq 0$. However, there is also some significant longshore motion for $dD_0/dy = 0.0275-0.055$ and insignificant rotation for negative dissipation gradients.

The drifter circulation patterns averaged over A_m/A_r classes are plotted in Fig. 14. There is a systematic progression from dominant alongshore flow for low values of A_m/A_r to strongly constrained circulatory flow for high values of A_m/A_r. Strong significant circulation is activated when the morphological area of the rip channel forms $>50\%$ of the total morphological area available for flow.

While it is clear that dD_0/dy and A_m/A_r display varying ability to differentiate between rip circulation and longshore flow, it is also useful to determine whether they can be used to quantify rip speed U_r. Using the previous class divisions of dD_0/dy and A_m/A_r, U_r was averaged across two longshore transects, one bisecting the main rip channel ($X = 650$ m) and one the rip neck region ($X = 690$ m) (Fig. 15). There is some trend in U_r based on the significant dD_0/dy observations for both locations, while for A_m/A_r, U_r is fairly consistent in the rip channel; however, across the rip neck U_r peaks for $A_m/A_r = 50-70\%$ before dropping again for $A_m/A_r > 70\%$. This is a similar observation to the circulation in Fig. 14, where the largest eddies are located in the $A_m/A_r = 50-70\%$ classes and the eddy becomes highly compacted and constrained in the highest class with a statistically significant reduction in rip speed.

5. Discussion

Detailed field measurements of the nearshore flow velocity field on a macro-tidal beach clearly demonstrate that rip current circulation is strongly modulated by the changing tidal elevation, which is the dominant temporal signal. In common with several previous studies (e.g. McKenzie, 1958; Sonu, 1972; Brander, 1999) the strongest rip flows are observed around low tide; outside of this low tide window, flows are predominantly alongshore. The tidal modulation is observed for both Eulerian and Lagrangian flow data.

The in situ flow velocity time series clearly show that strong offshore-directed flows ($\langle u \rangle = -0.5\,\mathrm{m\,s^{-1}}$) are activated once the local water depth falls below $\sim$ 3 m for the observed wave conditions. The longshore currents are similarly intensified

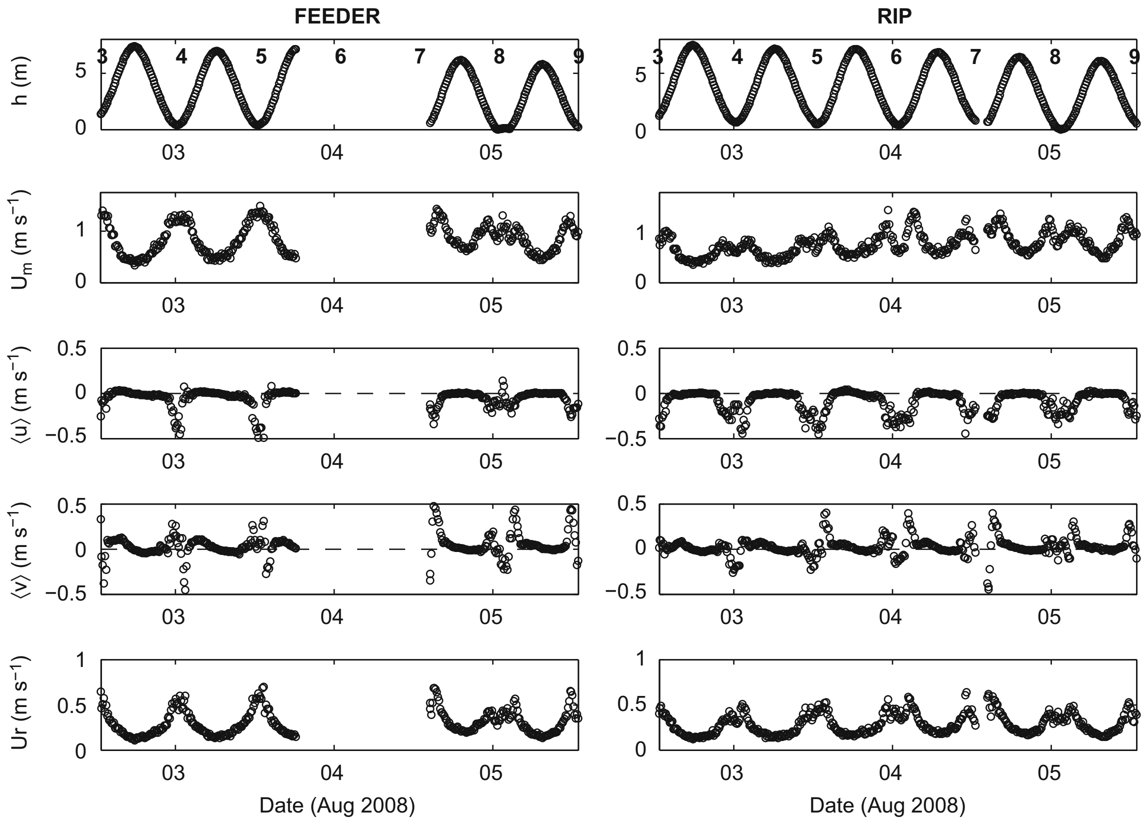

Fig. 8. Summary of the flow statistics measured by the in situ instruments. (From top) Water depth h; cross-shore orbital velocity U_m; mean cross-shore flow velocity $\langle u \rangle$, positive onshore; mean longshore flow velocity $\langle v \rangle$, positive north; and U_r mean return speed.

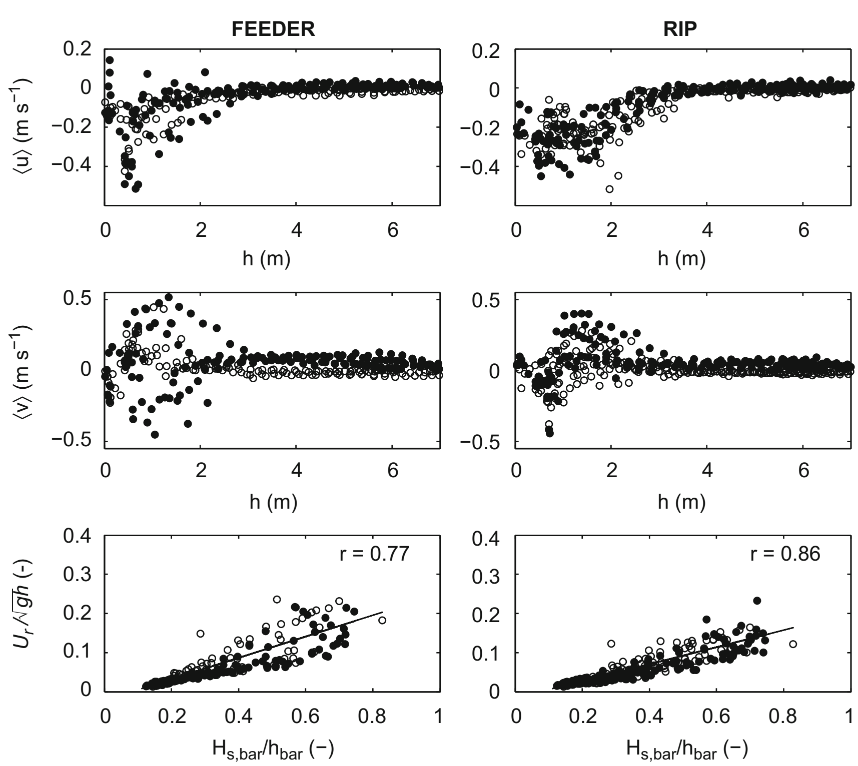

Fig. 9. Scatter plots of (top) mean cross-shore current vs. water depth; (middle) mean longshore current vs. water depth; and (bottom) Froude number $U_r/\sqrt{gh}$ vs. relative wave height H_s/h on the bar crest separated into flood (solid dots) and ebb (open circles) tide conditions. The solid line in the lower panels indicates the best linear fit.

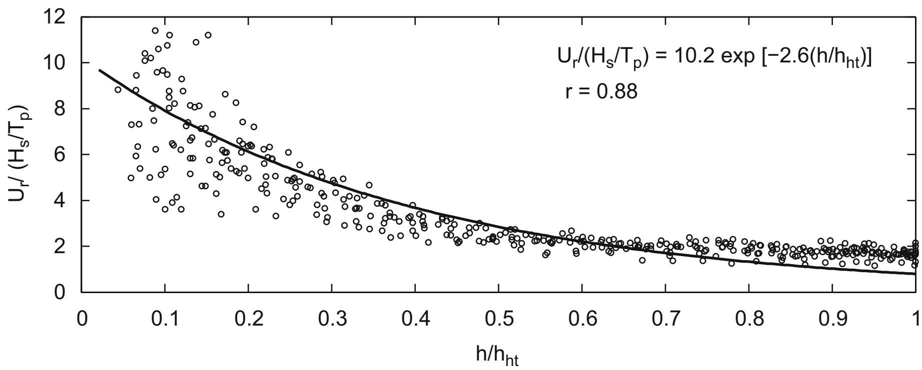

Fig. 10. Relationship between non-dimensional rip velocity $U_r/(H_s/T_p)$ and non-dimensional water depth h/h_{ht}. Solid line plots an exponential fit to the data as suggested by Brander and Short (2001).

around low water; however, these appear less directionally stable. This modulation is significantly more step-wise than previous observations of tidal modulation (e.g. Brander and Short, 2001) and indicates that in addition to the flow velocity modulation the rip is essentially being turned on and off by tidal-frequency water level variations, since for example the depth over the region of the rip is ~ 8 m at MHWS. The Lagrangian drifters demonstrate that the rip flows are rotational in nature. Wave-driven onshore flow over the bar crest transitions to an alongshore feeder-type current in the landwards trough, which flows into the base of the rip channel. The flow turns seaward and travels seawards through the surf zone under an angle between the two shore-attached bars. In common with other recent field observations (e.g. MacMahan et al., 2010a), this motion results in the formation of a large eddy, retained within the limits of the surf zone.

During this study, Perranporth exhibited pronounced TBR morphology combined with large tide ranges. The tide range modulated the expression of this morphology with two results: firstly, it caused a large variation in the spatial distribution of wave breaking; and secondly, resulted in morphological flow constriction.

The in situ data, supported by the wave roller dissipation, indicate that the rip begins to flow during the falling tide, from mid-tide downwards, corresponding to the initiation of depth-limited wave-breaking across the bar-crest. This is consistent with the findings of Sonu (1972) and Haller et al. (2002) amongst others, who provide strong evidence that wave breaking on the adjacent bars is required to drive rip circulation. It also highlights the transient nature of rip activity in a macro-tidal environment when compared to the observations of Brander and Short (2001), who measured a continual variation in rip velocity over the tidal cycle in a micro-tidal climate, in which there was persistent wave breaking throughout the tide. $H_{s,bar}/h_{bar}$ provides a reasonably good scaling of the rip speed explaining around 80% of the variance in the Eulerian measurements. However, for the Lagrangian observations, the similar dD_0/dy is not such a good discriminator of rip circulation with occasional, albeit potentially insignificant, rotational circulation being maintained during some periods when the dissipation gradient is directed away from the rip channel.

This discrepancy may be due to the emergence of the bar-crest around low water. For $H_{s,bar}/h_{bar}$, if the very shallow-water data (when the TWR was drying) could be included in the analysis, hysteresis would probably be observed whereby $H_{s,bar}/h_{bar}$ would decrease as both wave height and water depth tended toward zero at the shoreline, but U_r was maintained; the high correlation coefficients for the in situ data are therefore probably misleading. The occurrence of shallow uni-directional flow over the bar crest (Masselink et al., 2008) is one process that could maintain U_r towards low water, but significant side-drainage of water from the bars into the rip channel was also observed around low water and probably became an important process supplying water into the rip channel (Brander, 1999). For the Lagrangian observations utilising dD_0/dy, it is not clear why strong rip circulation is recorded during periods of limited wave dissipation into the flood tide phase of for example LT 5. During this period, the bar crest was fully submerged, dD_0/dy is reduced and yet the rip circulation continued into the flood tide period. This might be explained through a vorticity approach, whereby circulation is maintained by the torque that is generated by the radiation stress gradients (Bowen, 1969). Arthur (1962) indicates that vorticity is conserved along streamlines, which moving offshore become closer together creating a stronger current. This suggests that eddy vorticity may act to increase the relaxation timescale of the rip, maintaining rotation once the forcing is reduced.

A number of recent studies have linked vorticity to rotational circulation within the surf zone (e.g. MacMahan et al., 2001a, b) and Smith (2006) has demonstrated, through reformulating the momentum balance equations, that wave dissipation is important in forcing these vortical motions. Using this new formulation, Bonneton et al. (2010) find numerically that alongshore gradients in wave dissipation over transverse bar/rip morphology result in large-scale vorticity generation and surf zone rotations. Therefore although the high correlation between wave dissipation (parameterised as H_s/h_{bar}) and rip speed observed during this study is encouraging, in light of these new investigations, it is perhaps surprising that the correlation between dD_0/dy and rotational circulation is not higher.

Qualitative observations of the morphological control of the rip circulation suggest that as the water level decreases the increasing expression of the intertidal bars strongly channelise the flow. The alongshore flows are directed seawards by the relative emergence of the shore-connected shoal at the northern end of the rip system, flowing offshore towards the outer edge of the surf zone through the rip neck. It is at this point that the flow turns alongshore to the south before returning landwards over the inter-tidal bar crest. The circulation becomes strongly constrained as indicated by the drifter data for $A_m/A_r > 70\%$ and examination of the Argus video images indicates that the rip becomes an isolated hole-like region of no wave dissipation within the surf zone. It should be noted that there is no rip-head bar such as that described by Brander (1999) at the seaward end of the rip channel, and it is suggested that this bar has already welded to the seaward slope of the adjacent northern bar. This does, however, pose the question as to why there is a distinct band of wave breaking across the seaward extent of the rip channel and it

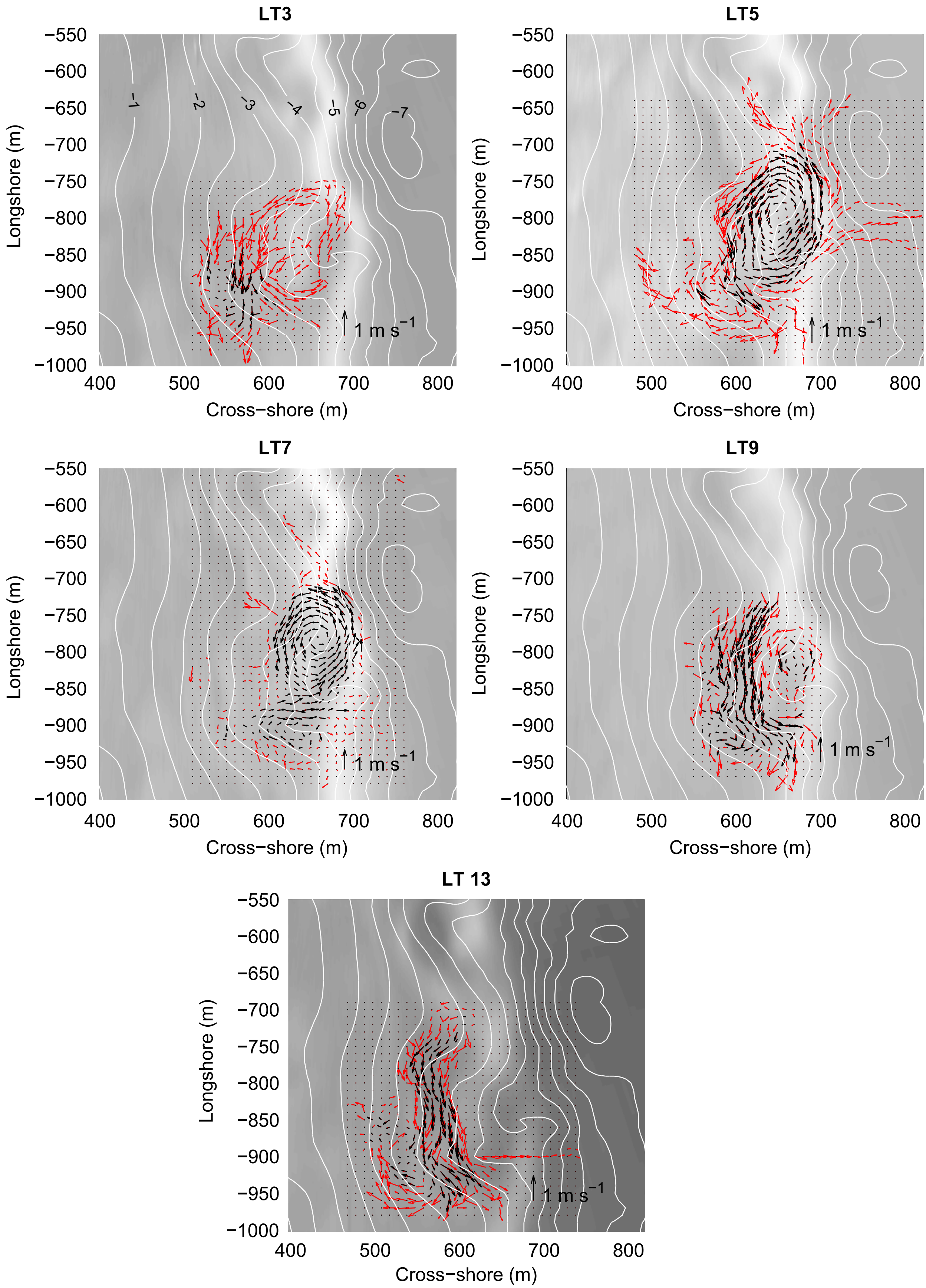

Fig. 11. Mean drifter velocity observations during each deployment. Vectors represent mean drifter direction and speed for all (red) and statistically significant (black) observations. Bathymetry is contoured at 0.5 m intervals, labelled in the upper left panel and the rectified low tide Argus timex image indicates wave breaking intensity in the background. (For interpretation of the references to colour in this figure legend, the reader is referred to the web version of this article.)

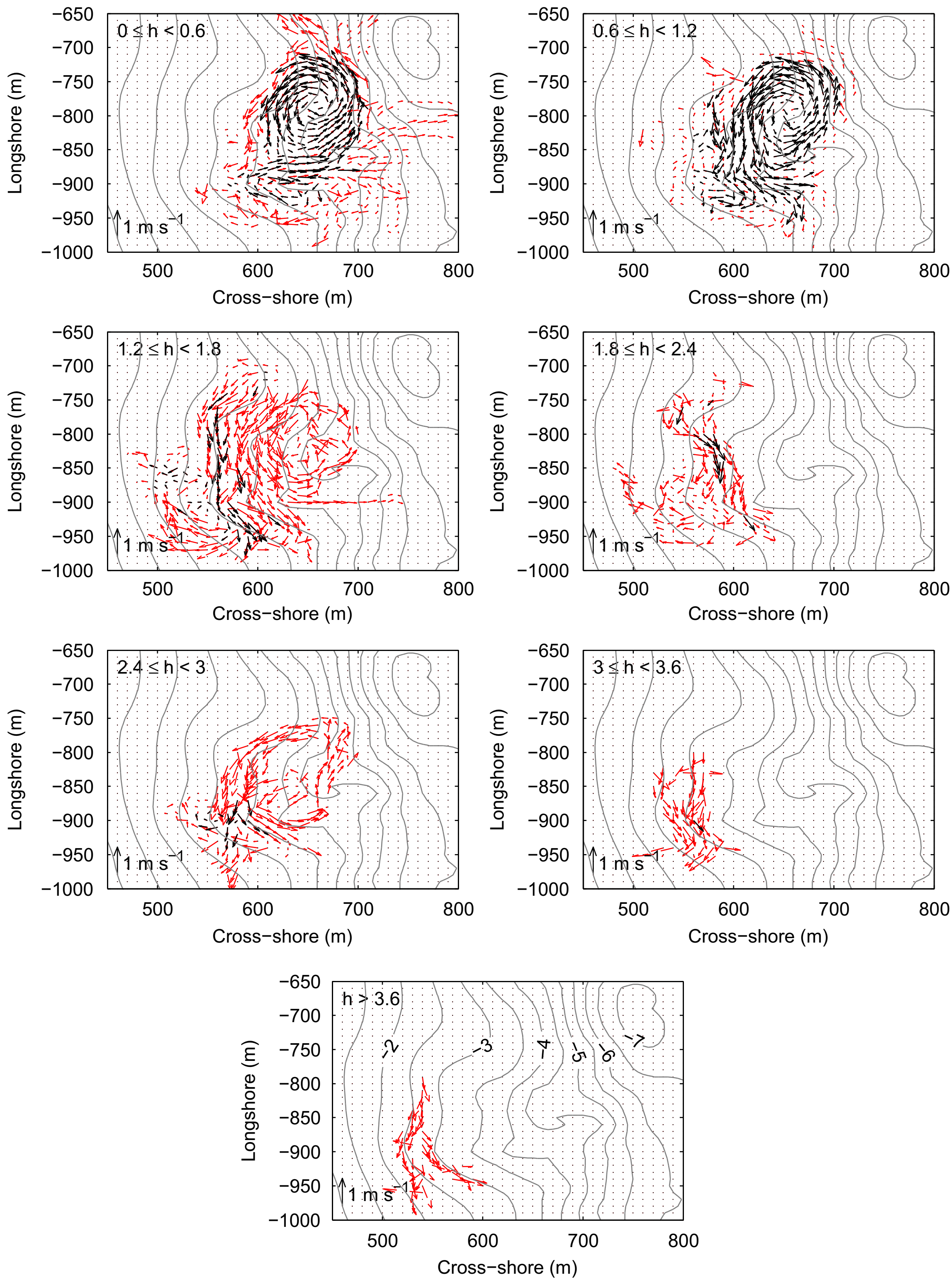

Fig. 12. Mean Lagrangian rip circulation separated into h_{bar} classes. Vectors represent rip speed within each spatial bin classified as statistically significant (> 5 independent observations, black) and all observations (red). Bathymetry is contoured in the background at 0.5 m intervals and labelled in the lower right panel. Rip speed is indicated by the scale arrow. (For interpretation of the references to colour in this figure legend, the reader is referred to the web version of this article.)

is suggested that this is due to wave–current interaction between the seaward-directed rip flows and landward wave propagation (Haller and Özkan Haller, 2002; Yu and Slinn, 2003; Reniers et al., 2007).

During this study morphological flow constriction was tidally modulated at the semi-diurnal and spring-neap timescales. The overall morphological configuration of the nearshore bars and troughs varies at the seasonal and storm-event timescales.

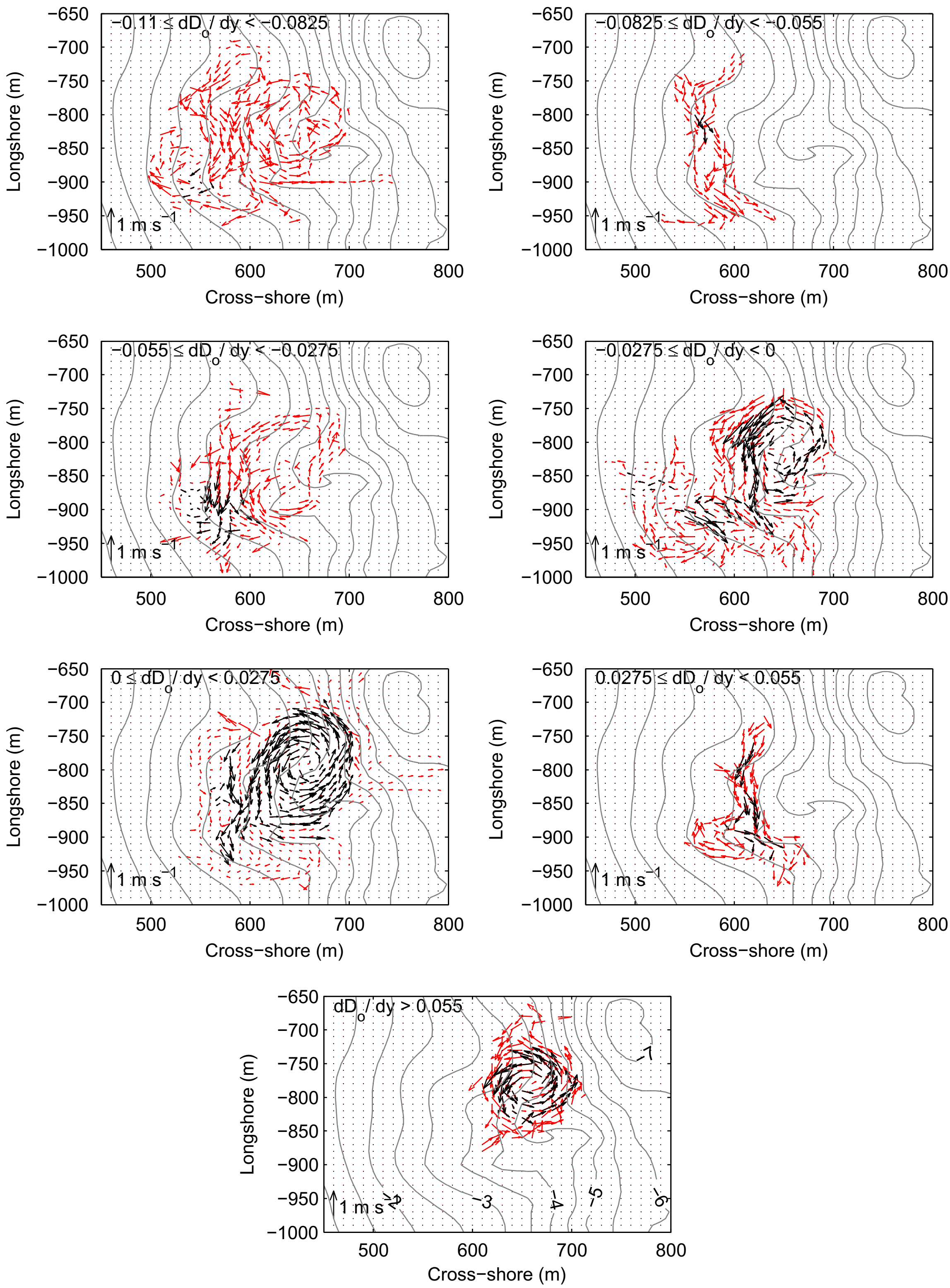

Fig. 13. Mean Lagrangian rip circulation separated into dD_0/dy classes. Vectors represent rip speed within each spatial bin classified as statistically significant (> 5 independent observations, black) and all observations (red). Bathymetry is contoured in the background at 0.5 m intervals and labelled in the lower left panel. Rip speed is indicated by the scale arrow. (For interpretation of the references to colour in this figure legend, the reader is referred to the web version of this article.)

Brander (1999) describes this variation in terms of morphological transitions during the accretionary phase of the Wright and Short (1984) beach-state model, during which there is a steady decrease in the cross-sectional area of the rip channel, infilling of the longshore feeder channels and an increase in rip flows. It is clear that during this experiment the reduction in tidal elevation around low water acts conceptually in the same manner as the wide-spread accretion during beach state changes at semi-diurnal frequencies. Fig. 16 illustrates the changing morphological relief during the falling tide of LT 5 through the ARGUS-derived roller

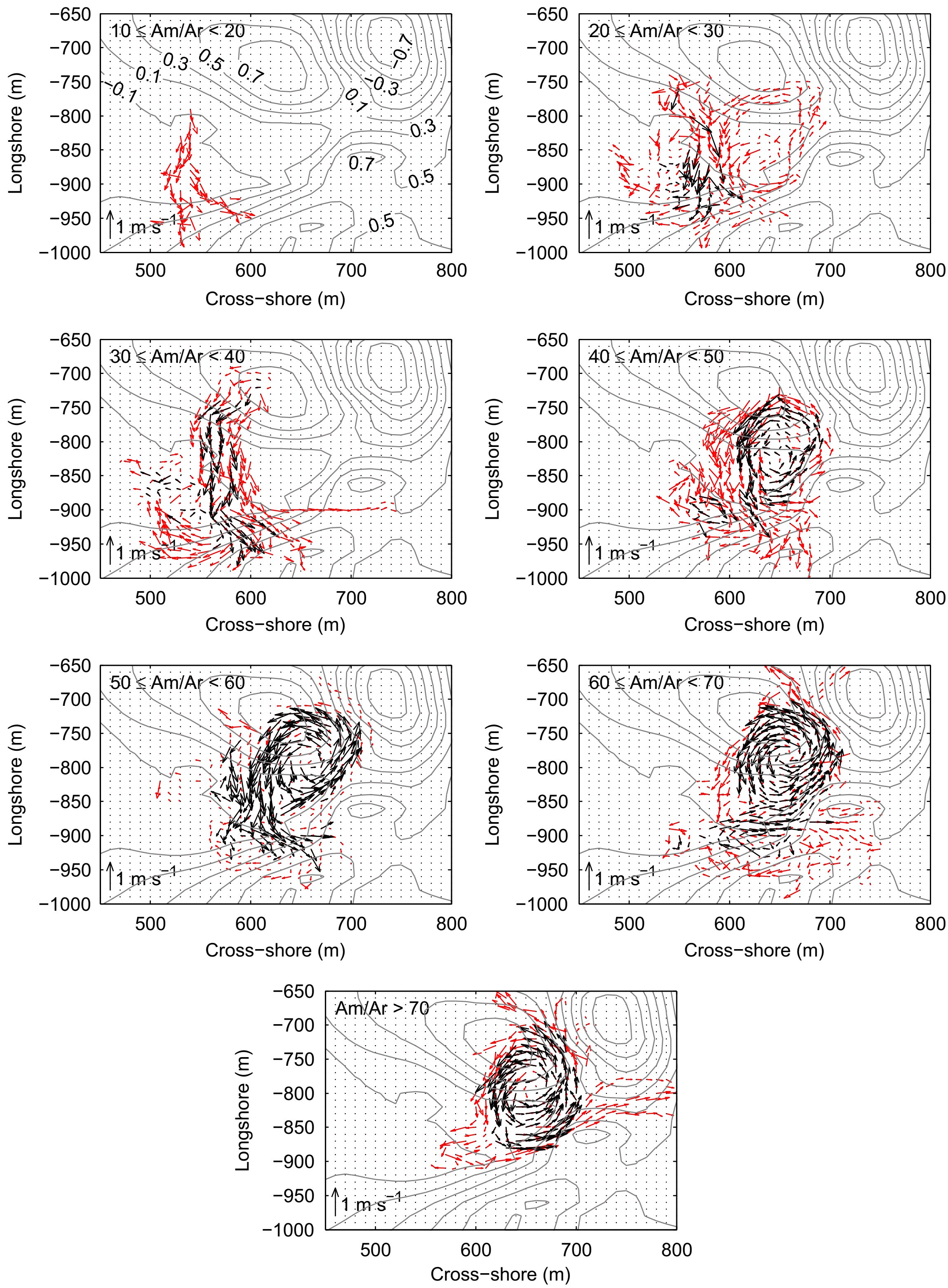

Fig. 14. Mean Lagrangian rip circulation separated into $\%(A_m/A_r)$ classes. Vectors represent rip speed within each spatial bin classified as statistically significant (>5 independent observations, black) and all observations (red). Residual bathymetry is contoured in the background at 0.2 m intervals and labelled in the upper left panel. Rip speed is indicated by the scale arrow. (For interpretation of the references to colour in this figure legend, the reader is referred to the web version of this article.)

dissipation maps. The 'effective' beach state progresses through the rhythmic bar-beach (RBB), RBB–TBR and TBR–low-tide terrace (LTT) states indicating that the falling water level acts to maximise bar relief, flow channelisation and rip speeds at the semi-diurnal timescale.

Further modulation of the rip occurs at the spring-neap timescale due to the reduction in tidal range from >6 m during springs to <3 m during neaps. The effect of this is twofold in that it influences both the dissipation and morphological control mechanisms. During the neap tide phase, greater water depths are

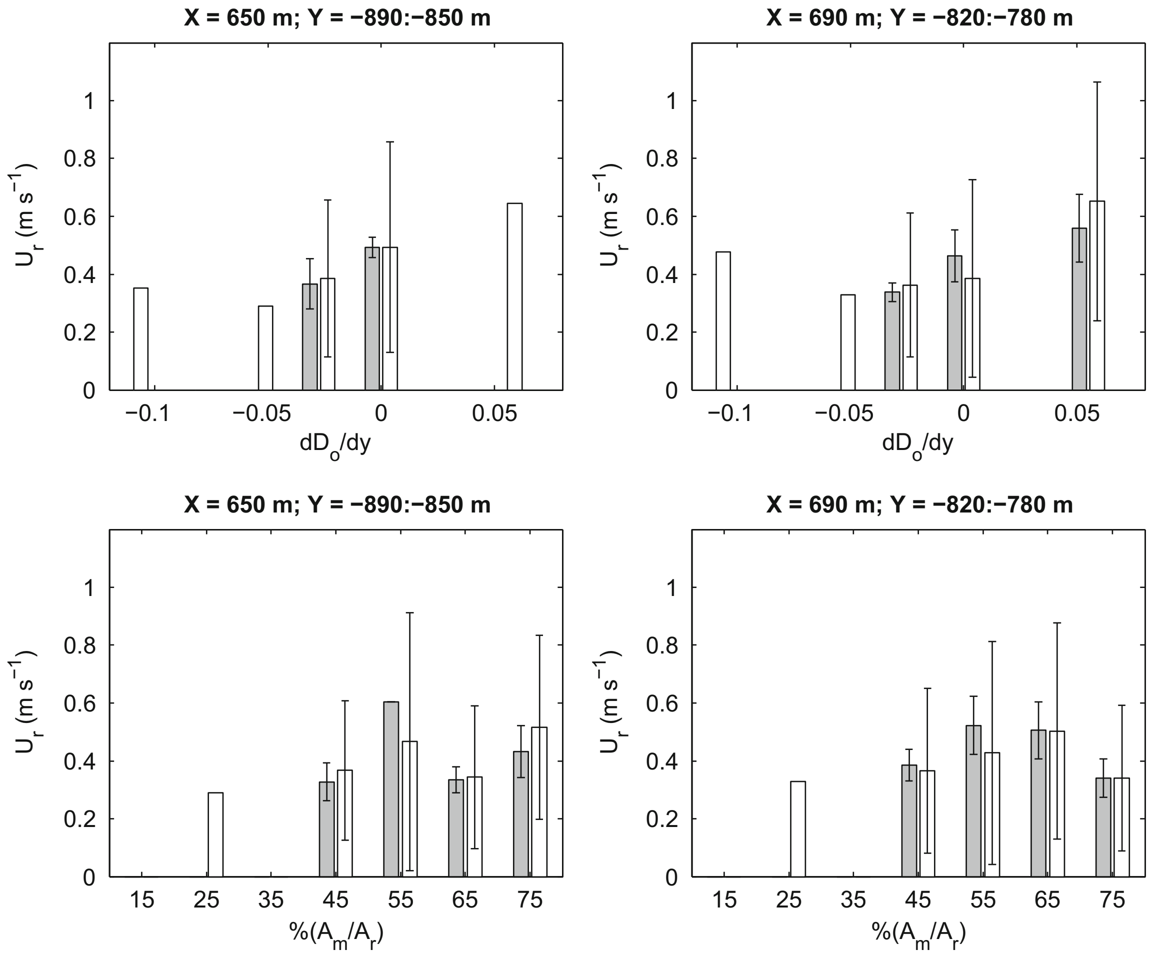

Fig. 15. Mean rip speed U_r across the rip channel (left) and rip neck (right) separated into dD_0/dy (top) and $\%(A_m/A_r)$ (bottom) classes. Solid bars include data with >5 independent observations and white bars include all observations. Errorbars plot the confidence intervals of the bars computed as $1.65\sigma/\sqrt{N}$, where σ is the standard deviation of each class and N is the number samples averaged within each class.

maintained over the inter-tidal bars during low tide minimising the morphological expression and reducing the intensity of depth-limited wave breaking. This was clearly evident during the later period of the field experiment, when limited morphological expression occurred during LT 9 and 13 and rip circulation was replaced by a longshore current. One explanation for the increased longshore current is the coincident decrease in tidal range and increased angle of wave approach during these tides (Table 1). Increased water depth over the sub- and inter-tidal bars allows waves to propagate further inshore, while reducing the amount of refraction. Waves continue to break over the inter-tidal bar and while the theoretical longshore current maxima should be located at the bar crest, it is probably diffused landwards into the trough by horizontal eddy mixing and through pressure gradients due to longshore variations in set-up over the bars (e.g. Symonds and Huntley, 1980; Larson and Kraus, 1991). This may therefore lead to a significant longshore current in the lee of the bar dominating over any cell circulation, whereas during spring tide periods, the longshore currents are more diffuse, since breaking and refraction over particularly the sub-tidal bar weakens the longshore momentum flux and the cell circulation dominates.

6. Conclusions

Field observations of rip current flows have been obtained to investigate their dynamic behaviour within a macro-tidal environment. This study has emphasised the strong tide-induced modulation of the rip flows and in common with previous investigations has highlighted that the strongest flow speeds occur around low water; moreover, it has indicated that there was a threshold depth of $h \simeq 3$ m, above which the rip flows appeared to cease under the wave conditions encountered during this study. Lagrangian drifters demonstrated that the rip current flow was strongly rotational, consisting of a large $O(200\,\text{m})$ eddy contained within the limits of the surf zone. During the high- and mid-tide periods when the rip was not active, longshore currents dominated. The results of this study also indicate that with the large spring-neap variations in tidal height, there are periods during the neap tides when water depths remain too deep to permit rip circulation over the existing morphology and again flows are primarily longshore.

The rip current dynamics appear to be controlled by a combination of wave dissipation and morphological flow constriction. Wave breaking over the inter-tidal bar crest was generally well correlated with rip flow speed and rip circulation peaked just before low water when the joint effects of dissipation and morphological constriction were maximised. The rip drifter data clearly indicate that the morphology was increasingly expressed when $A_m/A_r > 50\%$ and the system transitioned from the longshore-dominated to the rotational phase of the rip flow. At low tide, partial emergence of the bar crests probably reduced the effect of dissipation suggesting that morphological flow constriction becomes increasingly important in the shallowest water depths ($A_m/A_r > 70\%$).

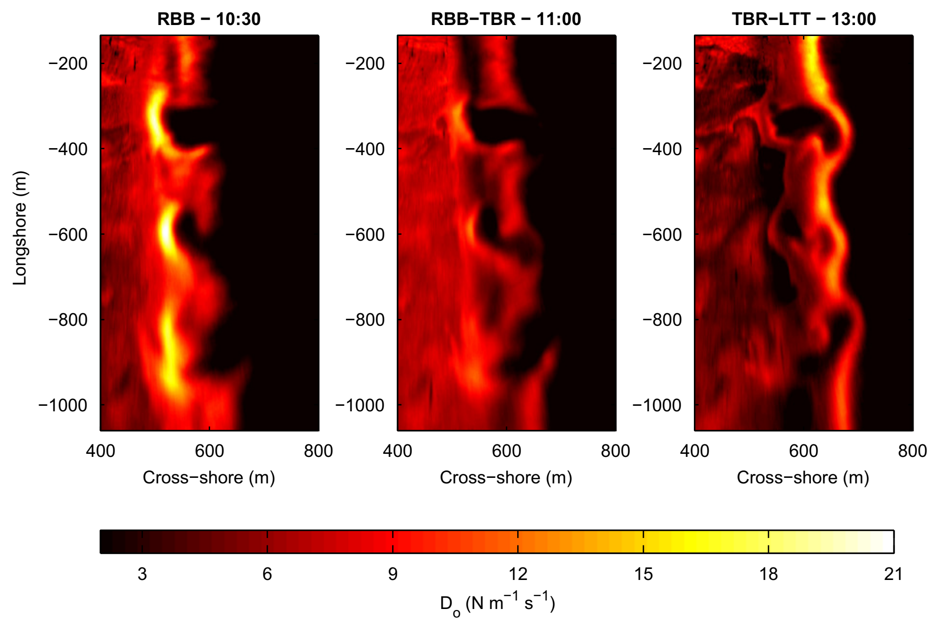

Fig. 16. Roller dissipation maps for LT 5 showing the progressive change in effective morphological beach state from RBB through to TBR–LTT during the falling tide.

Although this study has attempted to determine whether macro-tidal rip circulation can be attributed to either wave dissipation or morphological control, it seems that both processes ultimately combine to force the rip current. Variations in the pattern of wave dissipation and hence set-up gradients appear to trigger the rip circulation, but there are periods, particularly when water depths are very shallow and dissipation is limited to swash action over the bar crest, when morphological control appears to assume dominance. Flows became strongly canalised during this time with the circulation, which is maintained by side-drainage off the bars, constrained within the rip channel and rip neck regions.

Acknowledgements

We would like to thank our excellent field team Saul Reynolds, Iain Fairly, Tim Poate, Matt Hilton, Will Hibberd and James Moon for their efforts throughout the experiment. We are also indebted to the RNLI for their logistical support. Austin was supported by funds made available through the Wave Hub Impacts on Seabed and Shoreline Processes (WHISSP) project, funded by the Peninsular Research Institute for Marine Renewable Energy (PRIMaRE). Scott was supported by a HEIF2/RNLI award to the University of Plymouth. MacMahan was supported by ONR contract #N0001409WR20221, N0001409WR20222, and the NSF OCE 0728324. Brown (JW) was supported by the DE Sea Grant, U of Delaware and the NSF OCE 0728324. Brown (JA) was supported DE Sea Grant, U of Delaware and the NSF OCE 0728324.

References

Aagaard, T., Greenwood, B., Nielsen, J., 1997. Mean currents and sediment transport in a rip channel. Marine Geology 140 (1–2), 25–45.

Aarninkhof, S.G.J., Ruessink, B.G., Roelvink, J.A., Reniers, A.J.H.M., 2005. 2DH-quantification of surf zone bathymetry from video. In: Proceedings Coastal Dynamics '05, pp. 1–14.

Arthur, R.S., 1962. A note on the dynamics of rip currents. Journal of Geophysical Research 67 (7), 2777–2779.

Bonneton, P., Bruneau, N., Castelle, B., 2010. Large-scale vorticity generation due to dissipating waves in the surf zone. Discrete and Continuous Dynamical Systems—Series B 13 (4), 729–738.

Bowen, A.J., 1969. Rip currents. 1. Theoretical investigations. Journal of Geophysical Research 74, 5467–5478.

Bowman, D., Rosen, D.S., Kit, E., Arad, D., Slavicz, A., 1988. Flow characteristics at the rip current neck under low energy conditions. Marine Geology 79 (1–2), 41–54.

Brander, R., 1999. Field observations on the morphodynamic evolution of a low-energy rip current system. Marine Geology 157 (3–4), 199–217.

Brander, R.W., Short, A.D., 2000. Morphodynamics of a large-scale rip current system at Muriwai Beach, New Zealand. Marine Geology 165 (1–4), 27–39.

Brander, R.W., Short, A.D., 2001. Flow kinematics of low-energy rip current systems. Journal of Coastal Research 17 (2), 468–481.

Bruneau, N., Castelle, B., Bonneton, P., Pedreros, R., Almar, R., Bonneton, N., Bretel, P., Parisot, J.-P., Sénéchal, N., 2009. Field observations of an evolving rip current on a meso-macrotidal well-developed inner bar and rip morphology. Continental Shelf Research 29, 1650–1662.

Haller, M., Dalrymple, R., Svendesen, I., 2002. Experimental study of nearshore dynamics on a barred beach with rip channels. Journal of Geophysical Research 107 (14), 1–21.

Haller, M.C., Özkan Haller, H.T., 2002. Wave breaking and rip current circulation. In: Proceedings 28th International Conference on Coastal Engineering. ACSE, Cardiff, UK, pp. 705–717.

Huntley, D.A., Hendry, M.D., Haines, J., Greenidge, B., 1988. Waves and rip currents on a Caribbean pocket beach. Journal of Coastal Research 4 (1), 69–79.

Larson, M., Kraus, N.C., 1991. Numerical model of longshore current for bar and trough beaches. Journal of Waterway, Port, Coastal and Ocean Engineering 117, 326–347.

MacMahan, J.H., Thornton, E.B., Reniers, A.J.H.M., 2006. Rip current review. Coastal Engineering 53 (2–3), 191–208.

MacMahan, J.H., Brown, J.W., Brown, J.A., Morrison, J., Thornton, E.B., Reniers, A.J.H.M., Henriquez, M., Gallagher, E.L., Morrison, J., Austin, M.J., Scott, T.M., Sénéchal, N., 2010a. Mean Lagrangian flow behavior on an open coast rip-channeled beach. Marine Geology 268 (1-4), 1–15.

MacMahan, J.H., Reniers, A.J.H.M., Thornton, E.B., 2010b. Vortical surfzone velocity fluctuations with *O*(10) minute period. Journal of Geophysical Research, in press, doi:10.1029/2009JC005383.

MacMahan, J.H., Brown, J.W., Thornton, E.B., 2009. Low-cost hand-held global positioning system for measuring surfzone currents. Journal of Coastal Research 25 (3), 744–754.

MacMahan, J.H., Thornton, E.B., Stanton, T.P., Reniers, A.J.H.M., 2005. RIPEX: observations of a rip current system. Marine Geology 218 (1–4), 113–134.

Masselink, G., Austin, M.J., Tinker, J., O'Hare, T., Russell, P.E., 2008. Cross-shore sediment transport and morphological response on a macro-tidal beach with intertidal bar morphology, Truc Vert, France. Marine Geology 251, 141–155.

Masselink, G., Short, A.D., 1993. The effect of tide range on beach morphodynamics and morphology. Journal of Coastal Research 9, 785–800.

McKenzie, P., 1958. Rip-current systems. Journal of Geology 66 (2), 103–113.

Reniers, A.J.H.M., MacMahan, J.H., Thornton, E.B., Stanton, T.P., 2007. Modeling very low frequency motions during ripex. Journal of Geophysical Research 112(C07013), doi:10.1029/2005JC003122.

Ruessink, B.G., Houwman, K.T., Hoekstra, P., 1998. The systematic contribution of transporting mechanisms to the cross-shore sediment transport in water depths of 3–9 m. Marine Geology 152, 295–324.

Schmit, W.B., Woodward, K., Millikan, R., Guza, R.T., Raubenheimer, B., Elgar, S., 2003. A GPS-tracked surf zone drifter. Journal of Atmospheric and Ocean Technology 20, 1069–1075.

Scott, T.M., Russell, P.E., Masselink, G., Wooler, A., 2008. High volume sediment transport and its implications for recreational beach risk. In: Proceedings 31st International Conference on Coastal Engineering. ASCE, Hamburg, Germany, pp. 4250–4262.

Scott, T.M., Russell, P.E., Masselink, G., Wooler, A., 2009. Rip current variability and hazard along a macro-tidal coast. Journal of Coastal Research SI 56, 895–899.

Scott, T.M., Russell, P.E., Masselink, G., Wooler, A., Short, A.D., 2007. Beach rescue statistics and their relation to nearshore morphology and hazards: a case study for southwest England. Journal of Coastal Research SI 50, 1–6.

Shepard, F.P., Emery, K.O., LaFond, E.C., 1941. Rip currents: a process of geological importance. Journal of Geology XLIX, 337–369.

Short, A.D., 1985. Rip-current type, spacing and persistence, Narrabeen Beach, Australia. Marine Geology 65(1–2), 47–71.

Short, A.D., Brander, R.W., 1999. Regional variations in rip density. Journal of Coastal Research 15 (3), 813–822.

Smith, J.A., 2006. Wave-current interactions in finite depth. Journal of Physical Oceanography 36, 1403–1419.

Sonu, C.J., 1972. Field observation on nearshore circulation and meandering currents. Journal of Geophysical Research 77, 3232–3247.

Spydell, M., Feddersen, F., Guza, R.T., Schmit, W.E., 2007. Observing surf-zone dispersion with drifters. Journal of Physical Oceanography 37 (12), 2920–2939.

Symonds, G., Huntley, D.A., 1980. Waves and currents over nearshore bar systems. In: Proceedings of the Canadian Coastal Conference. National Research Council, Canada, pp. 64–78.

van Dongeren, A., Plant, N., Cohen, A., Roelvink, J.A., Haller, M., Catalán, P., 2008. Beach wizard: nearshore bathymetry estimation through assimilation of model computations and remote observation. Coastal Engineering 55, 1016–1027.

Wright, L.D., Short, A.D., 1984. Morphodynamic variability of surf zones and beaches: a synthesis. Marine Geology 56, 93–118.

Yu, J., Slinn, D.N., 2003. Effects of wave-current interaction on rip currents. Journal of Geophysical Research 108, 3088 , doi:10.1029/2001JC001105.